INTERNATIONAL JOURNAL FOR NUMERICAL METHODS IN FLUIDS, VOL. 19, 939–956 (1994)

COMPUTATION OF CONFINED COFLOW JETS WITH THREE TURBULENCE MODELS

J. ZHU AND T.-H. SHIH

Institute for Computational Mechanics in Propulsion and Center for Modeling of Turbulence and Transition, NASA Lewis Research Center, Cleveland, OH 44135, U.S.A.

SUMMARY

A numerical study of confined jets in a cylindrical duct is carried out to examine the performance of two recently proposed turbulence models: an RNG-based K–ε model and a realizable Reynolds stress algebraic equation model. The former is of the same form as the standard K–ε model but has different model coefficients. The latter uses an explicit quadratic stress–strain relationship to model the turbulent stresses and is capable of ensuring the positivity of each turbulent normal stress. The flow considered involves recirculation with unfixed separation and reatachment points and severe adverse pressure gradients, thereby providing a valuable test of the predictive capability of the models for complex flows. Calculations are performed with a finite volume procedure. Numerical credibility of the solutions is ensured by using second-order-accurate differencing schemes and sufficiently fine grids. Calculations with the standard K-ε model are also made for comparison. Detailed comparisons with experiments show that the realizable Reynolds stress algebraic equation model consistently works better than does the standard K–ε model in capturing the essential flow features, while the RNG-based K–ε model does not seem to give improvements over the standard K–ε model under the flow conditions considered.

KEY WORDS Turbulence models Confined jets Recirculation

1. INTRODUCTION

The flow configuration considered in this paper is sketched in Figure 1. It involves an inner high-speed round jet and a slowly moving annular stream, both interacting with each other. Because of turbulent entrainment, the jet increases its mass flux while spreading. This must be balanced by an equal decrease in the mass flux of the ambient flow. The decrease in the ambient velocity thus sets up an adverse pressure gradient which in turn affects the evolution of the flow. Depending on the ratio of jet to ambient velocities at the entrance, two different flow regimes occur in the downstream region: if the ratio is small, the jet cannot consume all the ambient flow before reaching the duct wall, so the flow remains unseparated; if the ratio is large, the opposite happens and further entrainment must create reverse flow to maintain the total mass flux conservation. Further downstream the flow completely loses its jet characteristics and degenerates eventually to the fully developed regime if the duct is long enough. These flow features can be found in many engineering apparatuses involving two flows of differing velocities, in particular in combustion chambers and ejectors. Therefore the understanding of confined jet flows is of great interest in engineering applications.

From a turbulence-modelling point of view, the confined jet flow also constitutes a valuable test owing to its complicated flow features. It is noted that the flow past a backward-facing step is a standard test problem to benchmark the performance of turbulence models in complex

CCC 0271–2091/94/220939–18

Received March 1994
Revised June 1994

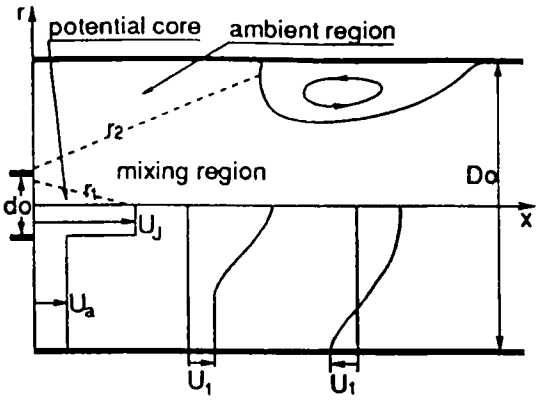

Figure 1. Flow configuration and notations

flows. The confined jet flow has features similar to those found in the backward-facing step flow, such as recirculation with an unfixed reattachment point and severe adverse pressure gradient, and adds additional complexities arising from the motion of the separation point.

Numerical calculations of confined jets have been reported by Gosman *et al.*,[1] Habib and Whitelaw,[2,3] Jones and Marquis,[4] Khalil *et al.*[5] and Zhu.[6] In these calculations, turbulence effects were represented either by the K–ε model or by second-moment closures. However, the previous calculations were all made on very coarse grids and with the hybrid central/upwind scheme,[7] which is highly diffusive in the presence of both convective dominance and flow-to-grid skewness. Therefore they might largely be contaminated by numerical diffusion and the results are far from conclusive.

The purpose of the present study is to assess the performance of two recently developed turbulence models in the confined jet flow. The models considered here are the RNG-based K–ε model used by Speziale and Thangam[8] and the realizable Reynolds stress algebraic equation (RRSAE) model,[9] both within the framework of the two-equation formulation. The RNG-based K–ε model is of the same form as the standard K–ε model[10] but assumes different model coefficients which are evaluated by the theory. In the original version of the RNG K–ε model all the coefficients had constant values which have been shown by Speziale and Thangam[8] to be inappropriate. In the latest version of the RNG K-ε model[8] the model coefficient related to the production-of-dissipation term in the ε-equation is a function of η, where η is the time scale ratio of the turbulent to mean strain rate. In the RRSAE model the Reynolds stresses are calculated by a quadratic stress–strain relation. All the model coefficients in this relation are determined from the realizability analysis so that the model ensures the positiveness of the turbulent normal stresses.

The test problem to be considered is taken from the experiment of Barchilon and Curtet,[11,12] which provides detailed experimental data. The flow can be characterized by the Craya–Curtet number C_t, which is the inverse square root of the total momentum, non-dimensionalized with the volume flux and the duct area.[13] The experiment showed that recirculation occurs when $C_t \leqslant 0{\cdot}96$. Calculations are carried out with a conservative finite volume method and on a numerically accurate basis. As a common practice, the calculation with the standard K–ε model is also included for comparison. Detailed comparison with experiments at five C_t-values clearly reveal the predictive capabilities of the models in these flows of great practical importance.

2. MATHEMATICAL FORMULATION

2.1. Governing equations

Incompressible, steady state, turbulent flows are governed by the Reynolds-averaged continuity and Navier–Stokes equations. In the polar–cylindrical co-ordinate system (x, r) shown in Figure 1, the conservative form of these equations can be written as

$$\frac{\partial rU}{\partial x} + \frac{\partial rV}{\partial r} = 0, \tag{1}$$

$$\frac{\partial}{\partial x}\left[r\left(UU - \nu\frac{\partial U}{\partial x}\right)\right] + \frac{\partial}{\partial r}\left[r\left(VU - \nu\frac{\partial U}{\partial r}\right)\right] = -\frac{r}{\rho}\frac{\partial p}{\partial x} + \frac{\partial}{\partial x}\left[r\left(\nu\frac{\partial U}{\partial x} + \frac{\tau_{11}}{\rho}\right)\right] + \frac{\partial}{\partial r}\left[r\left(\nu\frac{\partial V}{\partial x} + \frac{\tau_{12}}{\rho}\right)\right], \tag{2}$$

$$\frac{\partial}{\partial x}\left[r\left(UV - \nu\frac{\partial V}{\partial x}\right)\right] + \frac{\partial}{\partial r}\left[r\left(VV - \nu\frac{\partial V}{\partial r}\right)\right] = -\frac{r}{\rho}\frac{\partial p}{\partial r} + \frac{\partial}{\partial x}\left[r\left(\nu\frac{\partial U}{\partial r} + \frac{\tau_{12}}{\rho}\right)\right] + \frac{\partial}{\partial r}\left[r\left(\nu\frac{\partial V}{\partial r} + \frac{\tau_{22}}{\rho}\right)\right] - \frac{2\nu V}{r} - \frac{\tau_{33}}{\rho}, \tag{3}$$

where U and V are the axial and radial velocities respectively, p is the pressure, ν is the kinematic viscosity and ρ is the density. The Reynolds stresses τ_{ij} in (2) and (3) are calculated by using the following three turbulence models.

Standard K–ε model[10]

$$\frac{\tau_{ij}}{\rho} = \nu_t(U_{i,j} + U_{j,i}) - \tfrac{2}{3}K\delta_{ij}, \qquad \nu_t = C_\mu\frac{K^2}{\varepsilon}, \tag{4}$$

$$\frac{\partial}{\partial x}\left\{r\left[UK - \left(\nu + \frac{\nu_t}{\sigma_K}\right)\frac{\partial K}{\partial x}\right]\right\} + \frac{\partial}{\partial r}\left\{r\left[VK - \left(\nu + \frac{\nu_t}{\sigma_K}\right)\frac{\partial K}{\partial r}\right]\right\} = G - \varepsilon, \tag{5}$$

$$\frac{\partial}{\partial x}\left\{r\left[U\varepsilon - \left(\nu + \frac{\nu_t}{\sigma_\varepsilon}\right)\frac{\partial \varepsilon}{\partial x}\right]\right\} + \frac{\partial}{\partial r}\left\{r\left[V\varepsilon - \left(\nu + \frac{\nu_t}{\sigma_\varepsilon}\right)\frac{\partial \varepsilon}{\partial r}\right]\right\} = C_1 G\frac{\varepsilon}{K} - C_2\frac{\varepsilon^2}{K}, \tag{6}$$

where G is the production term of the turbulent kinetic energy,

$$G = \frac{1}{\rho}[\tau_{11}U_{1,1} + \tau_{22}U_{2,2} + \tau_{33}U_{3,3} + \tau_{12}(U_{1,2} + U_{2,1})], \tag{7}$$

the velocity gradients $U_{i,j}$ are calculated by

$$U_{1,1} = \frac{\partial U}{\partial x}, \qquad U_{2,2} = \frac{\partial V}{\partial r}, \qquad U_{3,3} = \frac{V}{r}, \qquad U_{1,2} = \frac{\partial U}{\partial r}, \qquad U_{2,1} = \frac{\partial V}{\partial x} \tag{8}$$

and the model coefficients are

$$C_\mu = 0{\cdot}09, \qquad C_1 = 1{\cdot}44, \qquad C_2 = 1{\cdot}92, \qquad \sigma_K = 1, \qquad \sigma_\varepsilon = 1{\cdot}3. \tag{9}$$

RNG K–ε model.[8] This is of the same form as the standard K–ε model but uses the coefficients

$$C_\mu = 0{\cdot}085, \qquad C_1 = 1{\cdot}42 - \frac{\eta(1-\eta/4{\cdot}38)}{1+0{\cdot}015\eta^3}, \qquad C_2 = 1{\cdot}68, \qquad \sigma_K = \sigma_\varepsilon = 0{\cdot}7179, \tag{10}$$

where

$$\eta = \frac{KS}{\varepsilon}, \qquad S = (2S_{ij}S_{ij})^{1/2}, \qquad S_{ij} = \tfrac{1}{2}(U_{i,j} + U_{j,i}). \tag{11}$$

RRSAE model[9]

$$\frac{\tau_{ij}}{\rho} = \nu_t(U_{i,j} + U_{j,i}) + T_{ij} - \tfrac{2}{3}K\delta_{ij}, \qquad \nu_t = C_\mu \frac{K^2}{\varepsilon}, \tag{12}$$

where

$$C_\mu = \frac{2/3}{A_1 + \eta + \gamma\xi}, \tag{13}$$

$$T_{ij} = -\frac{K^3}{(A_2+\eta^3)\varepsilon^2}\left[C_{\tau 1}(U_{i,k}U_{k,j} + U_{j,k}U_{k,i} - \tfrac{2}{3}\Pi\delta_{ij}) + C_{\tau 2}(U_{i,k}U_{j,k} - \tfrac{1}{3}\tilde{\Pi}\delta_{ij}) + C_{\tau 3}(U_{k,i}U_{k,j} - \tfrac{1}{3}\tilde{\Pi}\delta_{ij})\right], \tag{14}$$

$$\Pi = U_{k,l}U_{l,k}, \qquad \tilde{\Pi} = U_{k,l}U_{k,l}, \tag{15}$$

$$\xi = \frac{K\Omega}{\varepsilon}, \qquad \Omega = (2\Omega^*_{ij}\Omega^*_{ij})^{1/2}, \qquad \Omega^*_{ij} = (U_{i,j} - U_{j,i})/2 + 4\varepsilon_{mji}\omega_m, \tag{16}$$

ω_m is the rotation rate of the reference frame and the model constants are

$$C_{\tau 1} = -4, \qquad C_{\tau 2} = 13, \qquad C_{\tau 3} = -2, \qquad A_2 = 1000. \tag{17}$$

In the work of Shih *et al.*[9] and Zhu and Shih[14] the following two sets of values for A_1 and γ were tested:

$$A_1 = 5{\cdot}5, \qquad \gamma = 0, \tag{18}$$

$$A_1 = 1{\cdot}25, \qquad \gamma = 0{\cdot}9. \tag{19}$$

Both of them have been found to give almost identical predictions for the two backward-facing step flows. With (19), the rotational effect of the mean flow enters into C_μ. However, we have found in the present work that the values in (18) work better for the axisymmetric confined jets. Therefore the values in (18) are taken here. The K and ε in the RRSAE model are calculated with the same equations as in the standard K–ε model.

2.2. *Boundary conditions*

Four types of boundaries are present in the calculation, namely the inlet, outlet, axis of symmetry and solid wall. Among them, the inlet boundary conditions demand special attention because they have a considerable influence on the calculations.[15,16] Table I gives the inlet jet and ambient velocities taken from the experiment of Barchilon and Curtet.[11]

Table I. Inflow conditions

C_t	U_J (cm s^{-1})	U_a (cm s^{-1})
0·976	1293·6	84·48
0·714	1298·9	60·72
0·506	1253·8	39·81
0·305	1282·1	21·86
0·152	1296·2	7·42

The Craya–Curtet number C_t is calculated by

$$C_t = \frac{U_m}{[(U_J^2 - U_a^2)(d_o/D_o)^2 + (U_a^2 - U_m^2)/2]^{1/2}}, \tag{20}$$

where $D_o = 16$ cm, $d_o = 1{\cdot}2$ cm and U_m is the mean velocity of the section,

$$U_m = (U_J - U_a)(d_o/D_o)^2 + U_a. \tag{21}$$

In the potential core and the ambient region (Figure 1) the velocities are uniform and the turbulence level is very low, so the flow may be treated as potential. However, between the potential core and the ambient region there exists a thin shear layer from which the turbulent entrainment develops. The specification of the boundary conditions in this layer is non-trivial. In this work the parabolic entrance region (PER) scheme of Zhu *et al.*[15] is used. The PER scheme, which allows the fine resolution of the initial shear layer, was developed on the assumption that although the flow as a whole is elliptic, there exists a short region near the entrance where the flow is parabolic. A parabolic calculation is first carried out over a short distance between $x = 0$ and x_e, by using the mixing length model

$$\overline{uv} = -\nu_t \frac{\partial U}{\partial r}, \qquad \nu_t = C^2(r_2 - r_1)^2 \left|\frac{\partial U}{\partial r}\right|, \tag{22}$$

where r_1 and r_2 are the co-ordinates of the inner and outer edges of the initial shear layer respectively (Figure 1) and C is an empirical coefficient given by

$$C^2 = 0{\cdot}0042 + 0.004U_a/U_J, \quad 0 \leqslant U_a/U_J \leqslant 0{\cdot}2. \tag{23}$$

The results of the parabolic calculation are then used as the inlet conditions at $x = x_e$ for the elliptic calculation. The inlet values of K and ε are calculated by

$$K = -\overline{uv}/0{\cdot}3, \qquad \varepsilon = 0{\cdot}09K^2/\nu_t. \tag{24}$$

It was found[6] that the PER scheme gives satisfactory predictions in the parabolic entrance region and the elliptic calculations were insensitive to x_e provided that $1 < x_e/d_o < 3$.

The outlet boundary is placed at $x = 10D_o$, where fully developed flow conditions are assumed. Along the axis of symmetry the normal velocity component and the normal gradients of the other variables are set to zero. The standard wall function approach[10] is used to handle the wall boundary conditions.

2.3. *Numerical procedure*

The transport equations (1)–(3), (5) and (6) can be written in the general form

$$\frac{\partial}{\partial x}\left[r\left(U\phi - \Gamma_\phi \frac{\partial \phi}{\partial x}\right)\right] + \frac{\partial}{\partial r}\left[r\left(V\phi - \Gamma_\phi \frac{\partial \phi}{\partial r}\right)\right] = S_\phi, \tag{25}$$

where ϕ stands for U, V, K and ε, and Γ_ϕ and S_ϕ are the corresponding diffusive coefficient and source term respectively. For the momentum equations (2) and (3), S_ϕ also includes the cross-derivative diffusion terms and the quadratic terms T_{ij} in (14).

The system of equations (25) is solved with the finite volume approach. It uses non-staggered grids with all the dependent variables being stored at the geometric centre of each control volume. The velocity–pressure coupling is handled with the momentum interpolation procedure of Rhie and Chow[17] and the SIMPLEC algorithm of Van Doormal and Raithby.[18] To ensure both accuracy and stability of numerical solutions, the hybrid linear/parabolic approximation (HLPA) scheme[19] is used to approximate the convection terms of (25). It has been shown[20] that the HLPA scheme of second-order accuracy works nearly as well as the third-order-accurate SMART[21] and SHARP[22] schemes in eliminating the numerical diffusion while retaining the boundedness of numerical solutions. Consider a typical control volume centred at node C as shown in Figure 2. The HLPA scheme evaluates the value of ϕ at the cell face 'w' as

$$\phi_w = U_w^+ \phi_W + U_w^- \phi_C + \Delta\phi_w, \tag{26}$$

where

$$\Delta\phi_w = U_w^+ \alpha_w^+ (\phi_C - \phi_W) \frac{\phi_W - \phi_{WW}}{\phi_C - \phi_{WW}} + U_w^- \alpha_w^- (\phi_W - \phi_C) \frac{\phi_C - \phi_E}{\phi_W - \phi_E}, \tag{27}$$

$$U_w^+ \equiv \tfrac{1}{2}(1 + |U_w|/U_w), \qquad U_w^- \equiv 1 - U_w^+ \qquad (U_w \neq 0), \tag{28}$$

$$\alpha_w^+ = \begin{cases} 1 & \text{if } |\phi_C - 2\phi_W + \phi_{WW}| < |\phi_C - \phi_{WW}|, \\ 0 & \text{otherwise} \end{cases} \tag{29}$$

$$\alpha_w^- = \begin{cases} 1 & \text{if } |\phi_W - 2\phi_C + \phi_E| < |\phi_W - \phi_E|, \\ 0 & \text{otherwise.} \end{cases} \tag{30}$$

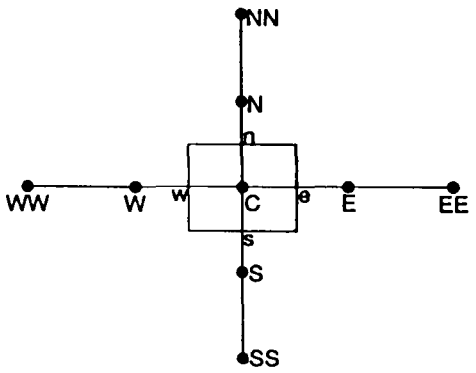

Figure 2. Control volume and related nodes

It can be seen that (26) is in fact the result of the first-order upwinding $U_w^+\phi_W + U_w^-\phi_C$ with an additional term $\Delta\phi_w$ added. The additional term may be viewed as an antidiffusive correction to the upwind scheme. The conventional central differencing scheme is used to approximate all other terms. The resulting discretized counterpart of (25) can be cast into the linearized form

$$A_C\phi_C = A_i\phi_i + S, \quad i = \text{W, E, S, N.} \tag{31}$$

In formulating this equation, the convection terms calculated by the upwind scheme are coupled with the normal diffusion terms to form the main coefficients A_i, while those calculated by (27) are included in the source term S. In this way the positivity of all the main coefficients is ensured so that the resulting coefficient matrix will always be diagonally dominant. The system of equations (31) is solved with the strongly implicit solution algorithm of Stone.[23] The calculation results are considered converged when the maximum normalized residue of all the dependent variables is less than 0·5%. The details of the present numerical procedure are given in References 24 and 25.

3. APPLICATION

All calculations were performed on the Cray YMP computer. The grid dependence of solutions was first examined by using two convection schemes, HLPA and HYBRID (central/upwind differencing), and three grids consisting of 50 × 40 (grid 1), 86 × 50 (grid 2) and 120 × 80 (grid 3) points respectively. The HYBRID scheme, which is highly diffusive in the presence of both convective dominance and flow-to-grid skewness, has been used here mainly to highlight the importance of using higher-order-accurate schemes. Test results obtained with the RRSAE model at $C_t = 0{\cdot}506$ are shown in Figure 3(a) for the axial velocity U-profiles, normalized by the mean velocity of the section, U_m, and in Figure 3(b) for the turbulent shear stress $\overline{uv}$-profiles, both at the same downstream location $x/D_o = 1{\cdot}875$. It can be seen that the results of HLPA on the coarse grid 1 are already very close to those on the fine grid 3 for both the U- and $\overline{uv}$-profiles, while significant differences exist between the corresponding results of HYBRID. The HLPA results on the intermediate grid 2 can be considered as grid-independent, because the refinement from grid 2 to grid 3 produced differences too small to be seen on the graph. The HYBRID solutions, however, responded to the grid refinement in such a slow manner that they still had not reached the grid-independent stage on the finest grid. The number of iterations and the CPU time in minutes required for the calculations with HLPA were respectively 196 and 0·2 on grid 1, 640 and 1·4 on grid 2 and 1874 and 9·3 on grid 3. The calculations with HYBRID took about 0·6–0·8 of these numbers. Grid 2 and HLPA were used for all subsequent calculations.

Figure 4 shows the variation in the centreline velocity U_o with x and C_t. It clearly reveals the existence of the potential core characterized by the constant U_o in the near-entrance region. Beyond the potential core U_o decayed quickly, especially at small values of C_t. Both the SKE model and the RNG model predicted the same potential core length, which was shorter than that predicted with the RRSAE model at all C_t-values. Since this length cannot be precisely determined from the first and second experimental points at each of C_t, it is difficult to judge which model gives the better initial decay ($x/D_o < 1$). For the ensuing decay the RRSAE model gave the best agreement with the experiment while the RNG model produced large under-predictions. Figures 5(a)–5(c) show the axial mean velocity profiles at three C_t-values. All three models are seen to predict very well the upstream evolution of the flow. As for the downstream development, the results obtained with the RRSAE model remained in good agreement with experiments, while those obtained with the other two models deteriorated, with the RNG model

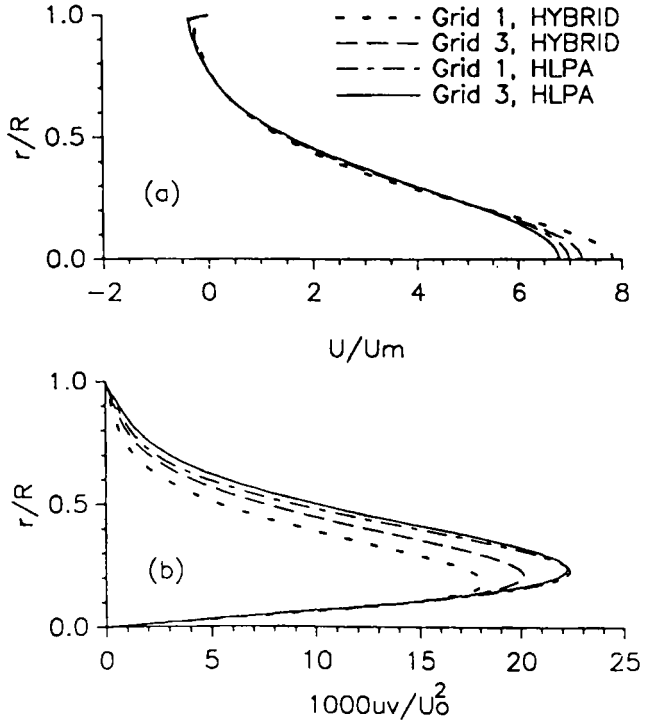

Figure 3. Grid sensitivity test at $C_t = 0{\cdot}506$

producing the largest discrepancies. The variation in the ambient velocity U_1 with x and C_t is shown in Figure 6. In the recirculation region the ambient velocity has no physical meaning and is defined as the minimum velocity (Figure 1) for analytical convenience. The location where U_1 is equal to zero corresponds to the separation or reattachment point. At $C_t = 0{\cdot}976$ the calculated results are shown only up to $x/D_o = 1{\cdot}875$, because the calculated U-profiles have no uniform portion after this point (Figure 5(a)). The calculated curves follow quite well the experimental data upstream of the separation at all C_t-values. The deviation occurs in the recirculation region. It should be pointed out that in the recirculation region the computed velocity minima are all very close to the duct wall, where the use of the wall function as the boundary condition may constitute a source of error. It is also to be noted that Figure 6 highlights considerably the difference between the computed and measured U-profiles in the near-wall region. The difference shown in Figures 5(b) and 5(c) is not significant as in Figure 6. Therefore the RRSAE model result should be considered as satisfactory.

The jet spreading can be characterized by the excess flow rate Q_j and the effective width l. These are defined by

$$Q_j = 2\pi \int_0^{r_2} (U - U_1) r \, dr, \qquad l^2 = \frac{Q_j}{\pi(U_o - U_1)}. \tag{32}$$

Figures 7 and 8 show the variation in Q_j/Q and l/R respectively with x and C_t, where Q and R are the total flow rate and the radius of the duct respectively. As a result of the turbulent entrainment, the excess flow rate first increases, reaches a maximum at the recirculation centre

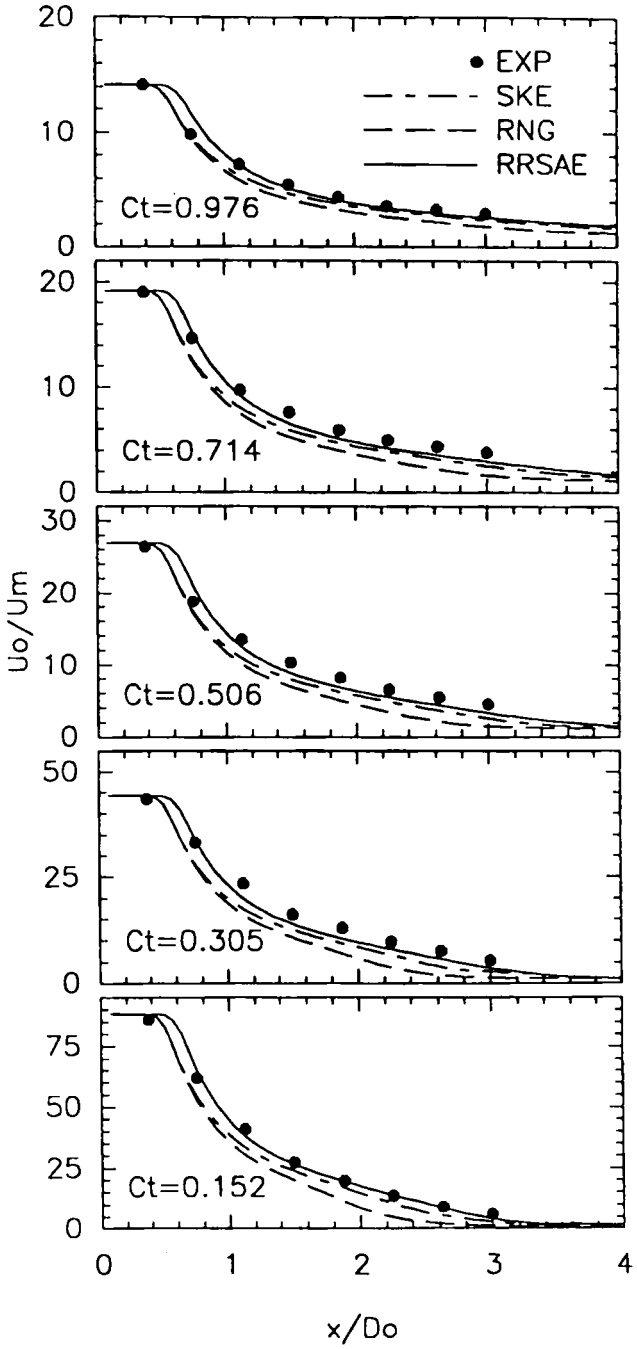

Figure 4. Centreline velocity decay

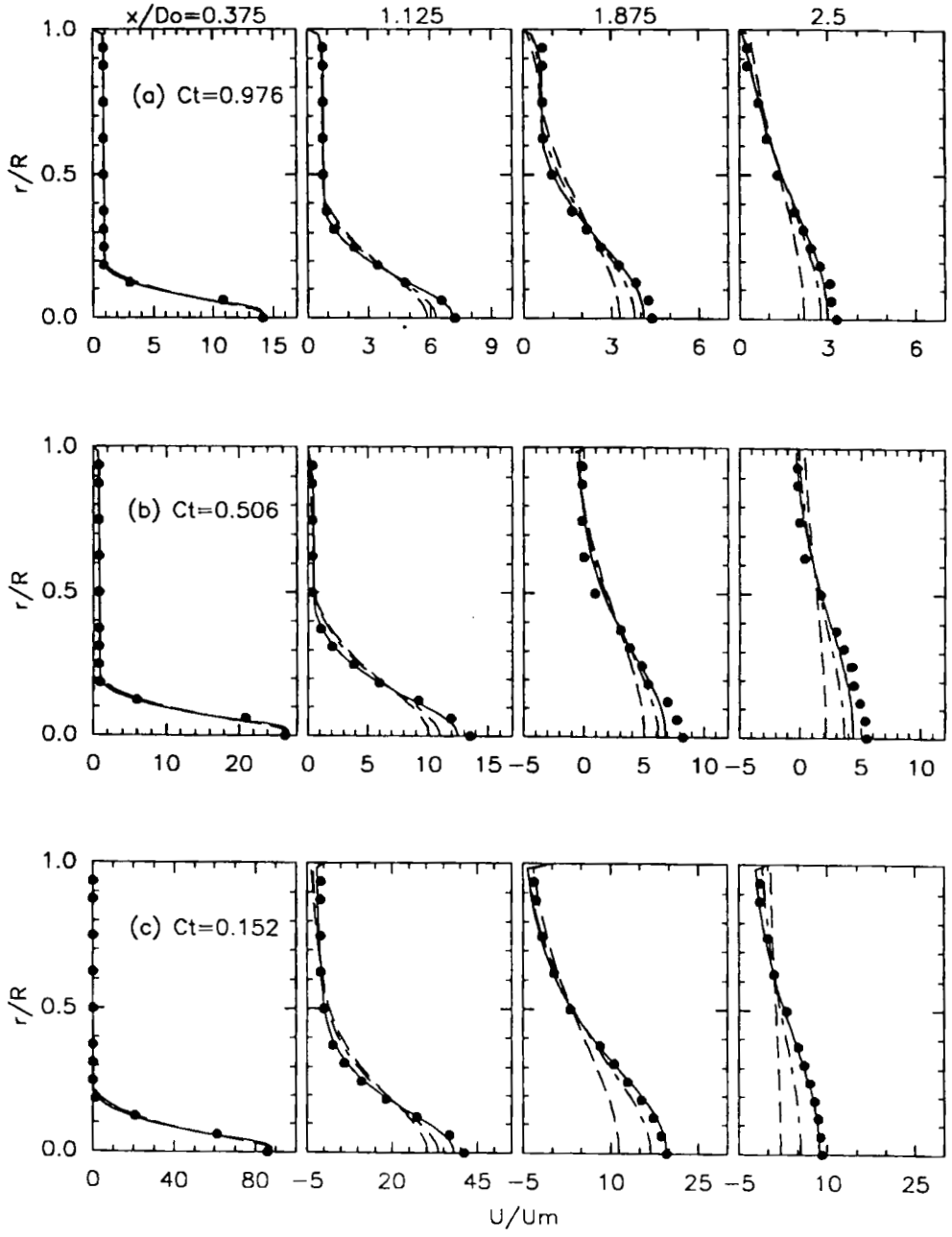

Figure 5. Axial mean velocity profiles (notation as in Figure 4)

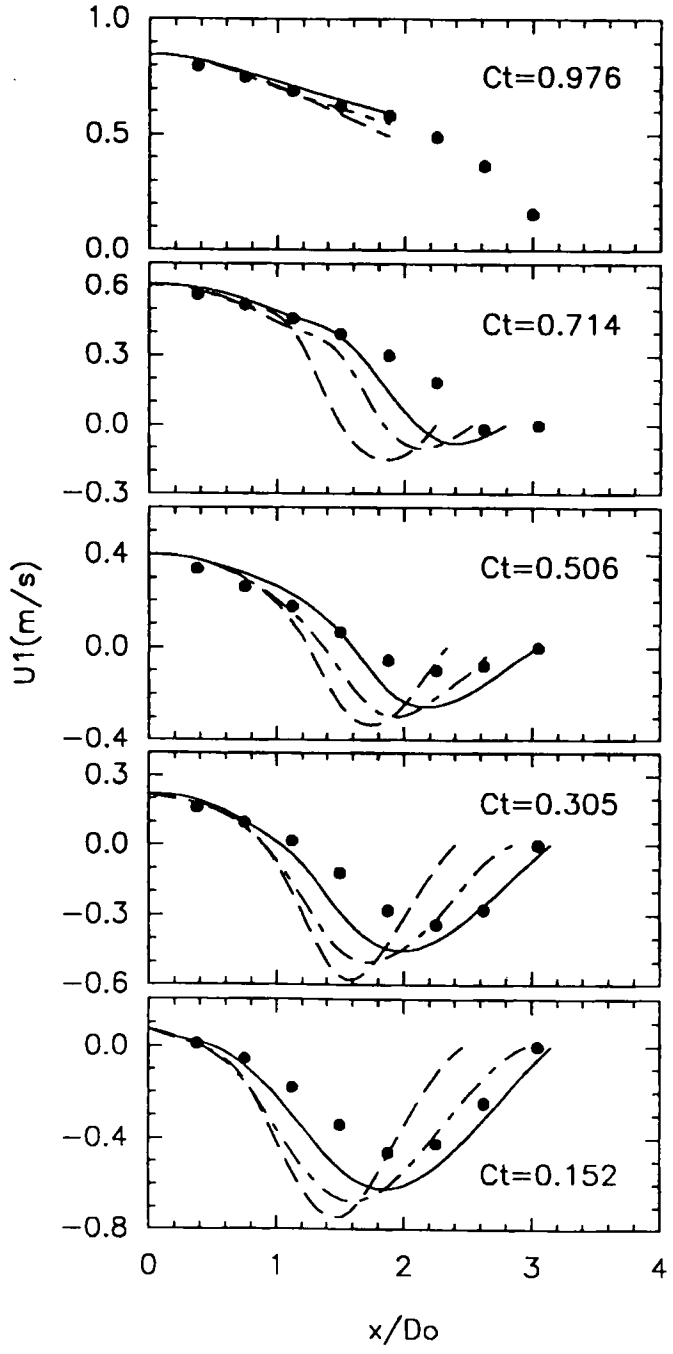

Figure 6. Ambient velocity (notation as in Figure 4)

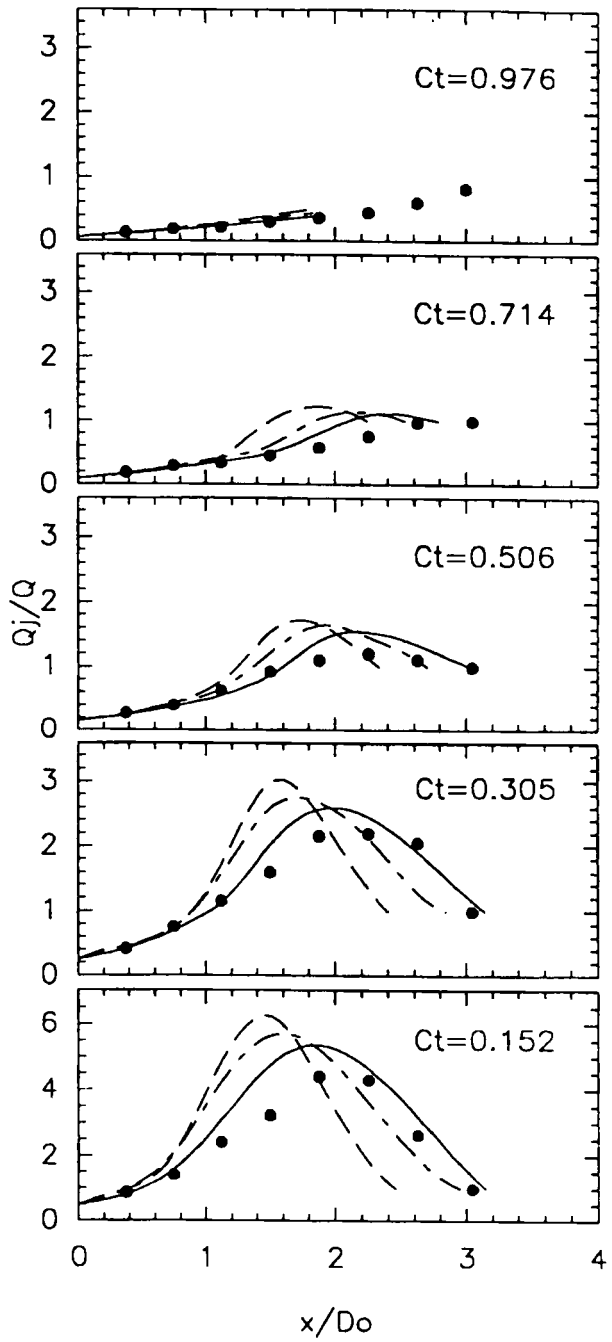

Figure 7. Excess flow rate (notation as in Figure 4)

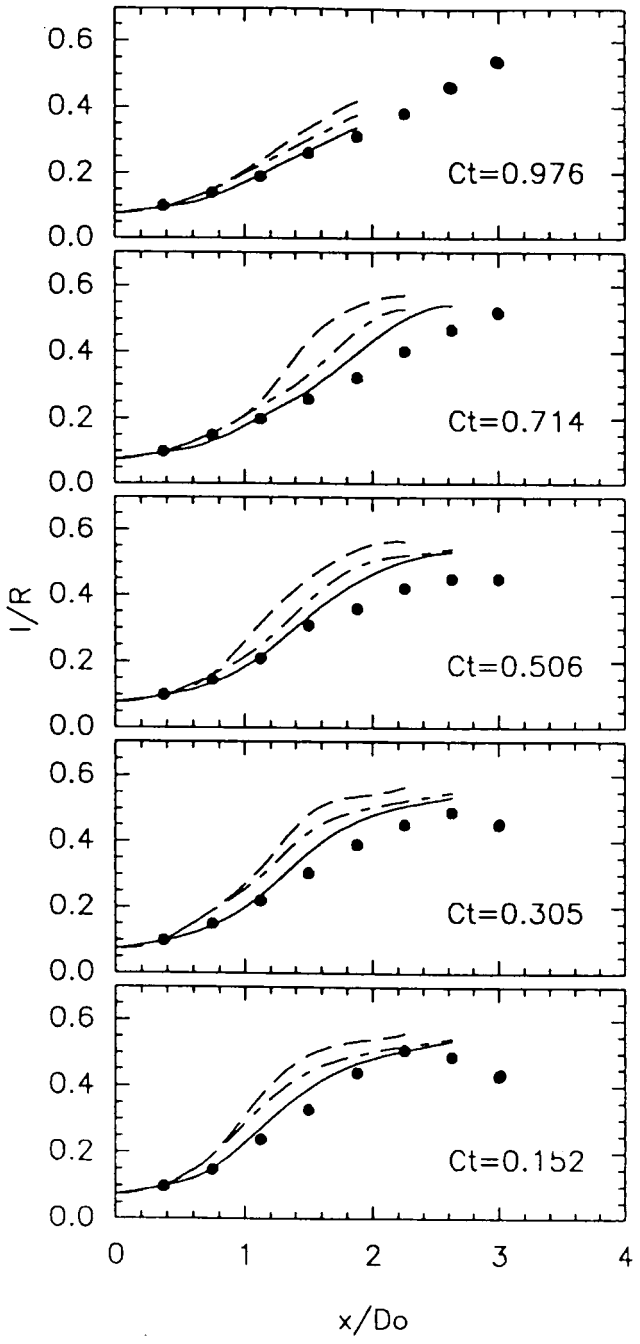

Figure 8. Effective width (notation as in Figure 4)

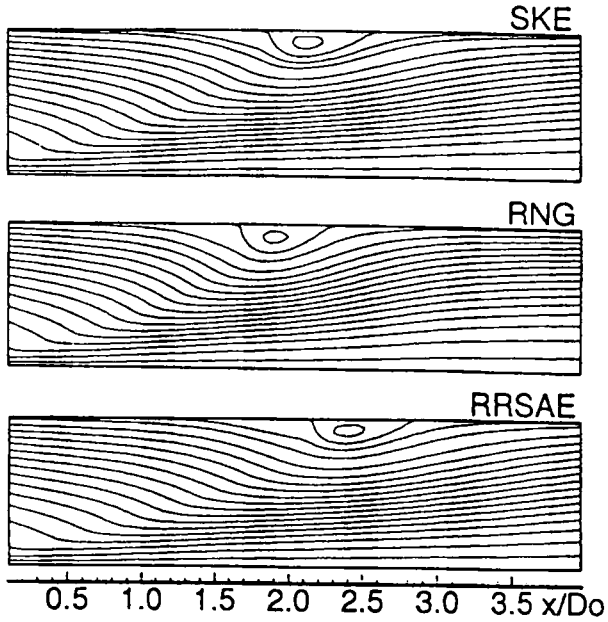

(a) Ct=0.714

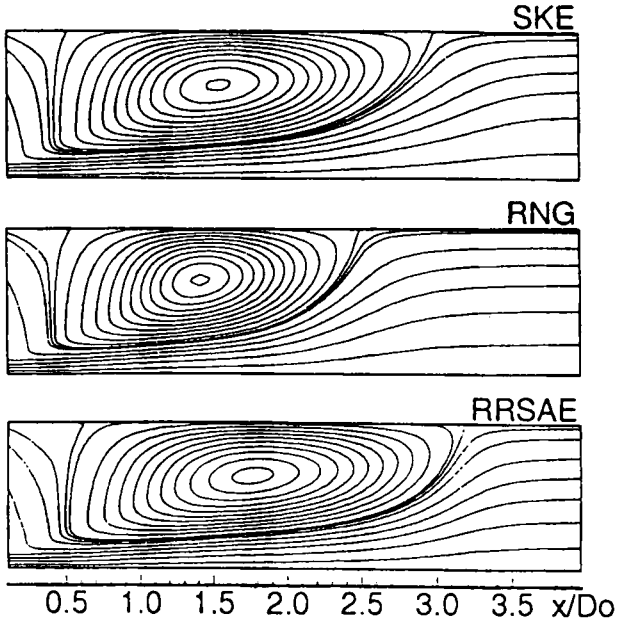

(b) Ct=0.152

Figure 9. Streamlines

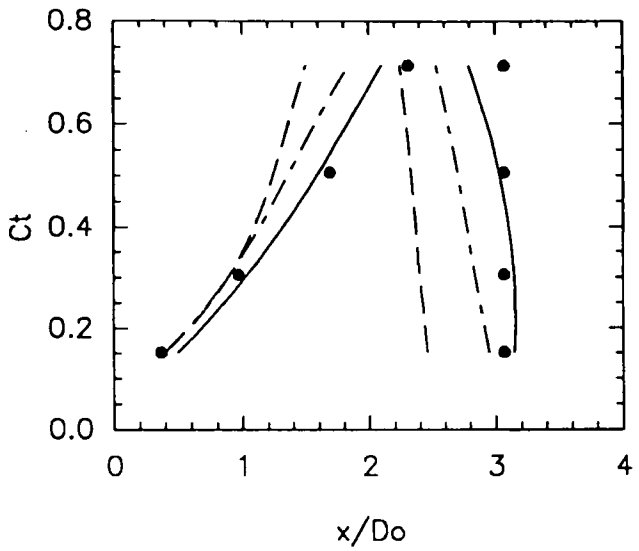

Figure 10. Separation and reattachment points (notation as in Figure 4)

where U_1 has a minimum and then decreases. This variation becomes more marked as C_t decreases. Recirculation occurs when Q_j is larger than Q. It can be seen from both figures that the calculations agree well with the experiments at larger C_t, but the agreement deteriorates as C_t decreases. It should be pointed out that the excess flow rate, owing to its definition, is a quantity that is highly sensitive to the errors in the velocity profiles, so that a small change in U_1, especially in the recirculation zone, will result in a large difference in Q_j. Furthermore, the experimental uncertainty in the recirculation region in which the flow is highly perturbed is likely to be greatest. With due regard to these factors, the agreement between the calculations and experiments can be regarded as reasonably good. Regarding the comparison among the three models, the RRSAE model again performs the best for both the excess flow rate and the effective width.

Figures 9(a) and 9(b) show the predicted streamlines at $C_t = 0{\cdot}714$ and $0{\cdot}152$ respectively. These figures convey an overall view of the flow pattern. The upstream ambient flow was sucked in by the jet owing to the turbulent entrainment. At $C_t = 0{\cdot}714$ a small recirculating bubble adhering to the duct wall occurred at the downstream location. When C_t was reduced to $0{\cdot}152$, the recirculating bubble became very large, filling most of the duct cross-section. The separation and reattachment points of the predicted recirculating bubbles are compared with the experimental data in Figure 10. The experiment indicated that as C_t decreased, the separation point moved upstream while the reattachment point remained practically unchanged. The comparison shows that the RRSAE model gives the best predictions for both the separation and reattachment points.

Figure 11 shows the variation in the recirculating flow rate with x at $C_t = 0{\cdot}305$ and $0{\cdot}152$. This is the integral of negative velocities in each cross-section. The experiment indicated that the recirculating flow rate at $C_t = 0{\cdot}152$ is about three times larger than that at $C_t = 0{\cdot}305$. The results of the RRSAE model are in good agreement with the experiment, while those of the standard K–ε model and the RNG model have substantial discrepancies. As for the maximum recirculating flow rate, which is a critical parameter to characterize the performance of

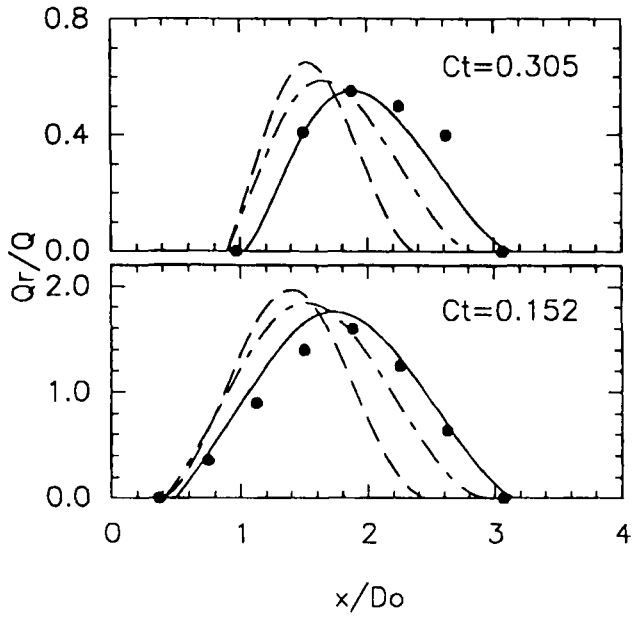

Figure 11. Recirculating flow rate (notation as in Figure 4)

combustion chambers, the RRSAE model gave the same result as the experimental data at $C_t = 0{\cdot}305$ and a 9% overprediction at $C_t = 0{\cdot}152$, while the other two models produced larger overpredictions. It should be pointed out that results from different measurements[11] for this quantity showed considerable scatter at small C_t-values. The results of all three models are within the experimental scatter.

The variation in pressure coefficient C_p along the duct wall is shown in Figure 12, where C_p is defined by

$$C_p = \frac{\Delta p - \rho U_a^2/2}{\rho U_j^2/2} \tag{33}$$

and Δp is the pressure difference relative to the entrance. In the cylindrical duct the evolution of the pressure is governed by the jet entrainment as well as the contraction and expansion of the flow caused by the recirculating bubble. The decrease in the ambient velocity (Figure 6) induced by the entrainment gives rise to an adverse pressure gradient, while the contraction of streamlines produces the opposite effect. These two mechanisms interact more intensely with each other as C_t decreases, causing the pressure to vary little in the region upstream of the centre of the recirculating bubble. In the downstream part of the recirculating bubble the deceleration of the flow sets up an adverse pressure gradient, the slope of which becomes steeper as C_t decreases. Therefore the ability to capture the location of the recirculation centre will have a direct impact on the prediction of the pressure. By comparing Figure 12 with Figure 6, it can be seen that the three models capture the steep pressure gradients in the same way as they capture the ambient velocity minima. However, for the total pressure rise, an important parameter to the designer of jet pump devices, all three models are seen to give the same results, which are in excellent agreement with the measurement.

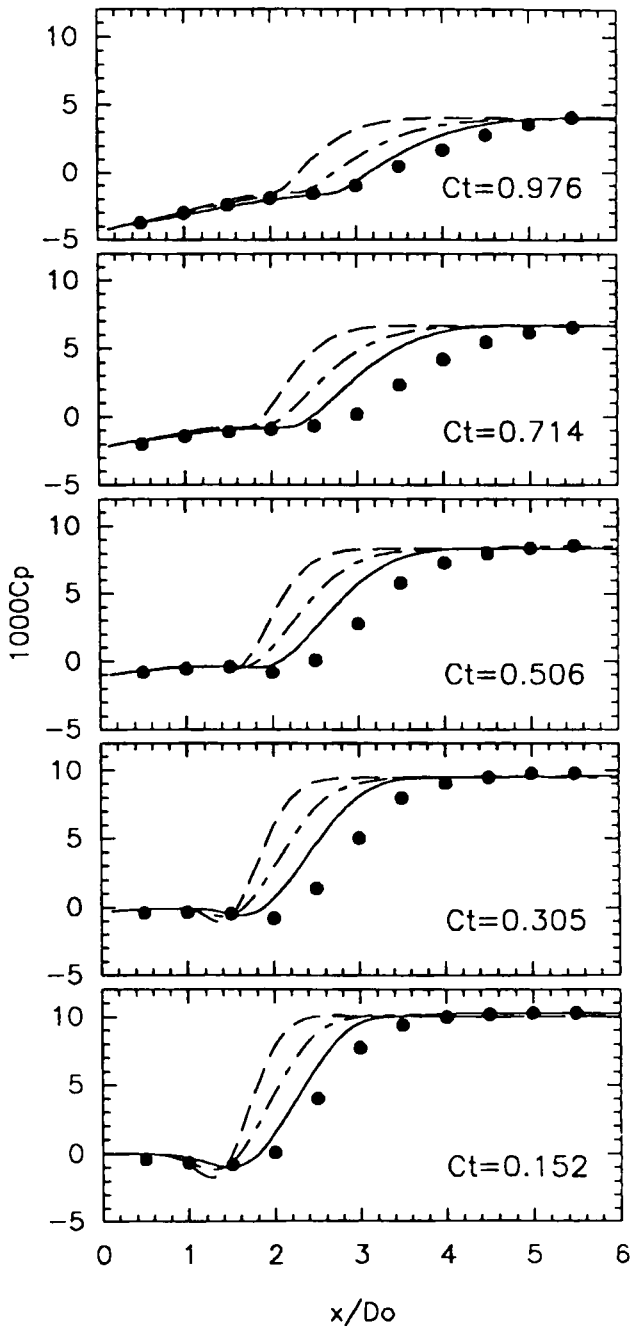

Figure 12. Pressure coefficient at wall (notation as in Figure 4)

4. CONCLUSIONS

A numerical study has been performed to assess two recently proposed turbulence models for confined jet flows. In order for the calculation to reflect the real performance of the models, an effort has been made to reduce numerical errors arising from the inlet boundary condition and numerical discretization. The detailed comparison with the experiment definitively establishes the superiority of the RRSAE model over the standard K–ε model in so far as the confined jet problem is concerned. However, this is not true for the RNG model at all the values of C_t considered.

REFERENCES

1. A. D. Gosman, E. E. Khalil and J. H. Whitelaw, 'The calculation of two-dimensional turbulent recirculating flows', in F. Durst, B. E. Launder, F. W. Schmidt and J. H. Whitelaw (eds), *Turbulent Shear Flows 1*, Springer, New York, 1979, pp. 237–255.
2. M. A. Habib and J. H. Whitelaw, 'Velocity characteristics of a confined coaxial jet', *J. Fluids Eng.*, **101**, 521–529 (1979).
3. M. A. Habib and J. H. Whitelaw, 'Calculations of confined coaxial-jet flows', *Proc. Turbulent Shear Flows 3*, Davis, CA, 1981, pp. 5.20–5.26.
4. W. P. Jones and A. J. Marquis, 'Calculation of axisymmetric recirculating flows with a second order turbulent model', *Proc. Turbulent Shear Flows 5*, Ithaca, NY, 1985, pp. 20.1–20.6.
5. E. E. Khalil, D. B. Spalding and J. H. Whitelaw, 'The calculation of local flow properties in two-dimensional furnaces', *Int. J. Heat Mass Transfer*, **18**, 775–791 (1975).
6. J. Zhu, 'Calcul des jets turbulents confinés avec recirculation', *Doctoral Dissertation*, Institut National Polytechnique de Grenoble, 1986.
7. D. B. Spalding, 'A novel finite difference formulation for differential expressions involving both first and second derivatives', *Int. j. numerical methods eng.*, **4**, 551–559 (1972).
8. C. G. Speziale and S. Thangam, Analysis of an RNG based turbulence model for separated flows', *NASA CR 189600*, 1992.
9. T.-H. Shih, J. Zhu and J. L. Lumley, 'A realizable Reynolds stress algebraic equation model', *NASA TM 105993*, 1993.
10. B. E. Launder and D. B. Spalding. 'The numerical computation of turbulent flows', *Comput. Methods Appl. Mech. Eng.*, **3**, 269–289 (1974).
11. M. Barchilon and R. Curtet, 'Some details of the structure of an axisymmetric confined jet with backflow', *J. Basic Eng.*, **86**, 777–787 (1964).
12. M. Barchilon, 'Contribution à l'étude des courants de retour engendrés par un jet confiné', *Publications Scientifiques et Techniques du Ministère de l'Air*, Paris, 1969.
13. R. Curtet, 'Sur l'écoulement d'un jet entre parois', *Publications Scientifiques et Techniques du Ministère de l'Air, No. 359*, Paris, 1960.
14. J. Zhu and T.-H. Shih, 'Calculations of turbulant separated flows', *NASA TM 106154*, 1993.
15. J. Zhu, G. Binder and J. L. Kueny, 'Improved predictions of confined jets with a parabolic computation of the entrance region', *AIAA J.*, **25**, 1141–1142 (1987).
16. J. Zhu and W. Rodi, 'Computation of axisymmetric confined jets in a diffuser', *Int. j. numer. methods fluids*, **14**, 241–251 (1992).
17. C. M. Rhie and W. L. Chow, 'A numerical study of the turbulent flow past an isolated airfoil with trailing edge separation', *AIAA J.*, **21**, 1525–1532 (1983).
18. J. P. Van Doormal and G. D. Raithby, 'Enhancements of the SIMPLE method for predicting incompressible fluid flows', *Numer. Heat Transfer*, **7**, 147–163 (1984).
19. J. Zhu, 'A low diffusive and oscillation-free convection scheme', *Commun. Appl. Numer. Methods*, **7**, 225–232 (1991).
20. J. Zhu, 'On the higher-order bounded discretization schemes for finite-volume computations of incompressible flows', *Comput. Methods Appl. Mech. Eng.*, **98**, 345–360 (1992).
21. P. H. Gaskell and A. K. C. Lau, 'Curvature-compensated convective transport: SMART, a new boundedness preserving transport algorithm', *Int. j. numer. methods fluids*, **8**, 617–641 (1988).
22. B. P. Leonard, 'Simple high-accuracy resolution program for convective modelling of discontinuities', *Int. j. numer. methods fluids*, **8**, 1291–1318 (1988).
23. H. L. Stone, 'Iterative solution of implicit approximations of multidimensional partial differential equations', *SIAM J. Numer. Anal.*, **5**, 530–558 (1968).
24. W. Rodi, S. Majumdar and B. Schönung, 'Finite-volume method for two-dimensional incompressible flows with complex boundaries', *Comput. Methods Appl. Mech. Eng.*, **75**, 369–392 (1989).
25. J. Zhu, 'FAST-2D: a computer program for numerical simulation of two-dimensional incompressible flows with complex boundaries', *Rep. 690*, Institute for Hydromechanics, University of Karlsruhe, 1991.